CHEMISTRY OF MATERIALS

ARTICLE

pubs.acs.org/cm

Mesoporous Cr_2O_3–Phosphomolybdic Acid Solid Solution Frameworks with High Catalytic Activity

Ioannis Tamiolakis,[†] Ioannis N. Lykakis,[‡,▽] Alexandros P. Katsoulidis,[§] Manolis Stratakis,[‡] and Gerasimos S. Armatas*[,†]

[†]Department of Materials Science and Technology and [‡]Department of Chemistry, University of Crete, Heraklion 71003, Crete, Greece

[§]Department of Chemistry, Northwestern University, Evanston, Illinois 60208, United States

Supporting Information

ABSTRACT: Mesoporous nanocomposite frameworks of chromium(III) oxide and 12-phosphomolybdic acid (PMA) compounds were prepared via a "nanocasting" method, using mesoporous silica SBA-15 as the template. Small-angle X-ray scattering, transmission electron microscopy, and nitrogen physisorption characterizations indicate that these materials possess a well-ordered hexagonal mesostructure with high content of PMA clusters (up to 63 wt %) and large internal surface area (up to 165 m^2 g^{-1}). The Keggin clusters are incorporated intact into the mesoporous walls forming a Cr_2O_3–PMA solid-solution structure, according to the X-ray diffraction and X-ray photoelectron and ultraviolet–visible light (UV/vis) spectroscopy. These Cr_2O_3–PMA nanocomposites demonstrated strong potential for green oxidative processes, exhibiting high catalytic activity and durability in oxidation of 1-phenylethanol using H_2O_2 as an oxidant.

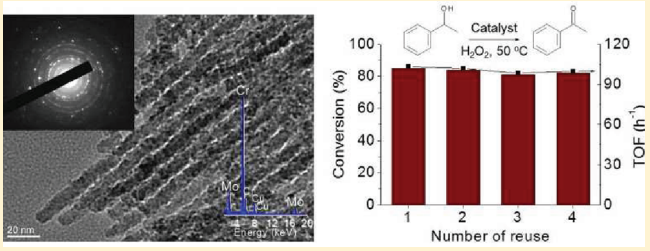

KEYWORDS: mesoporous materials, nanocomposites, chromium oxide, polyoxometalate, catalysis

INTRODUCTION

Nanostructured arrays of transition-metal oxides having large internal surface area and uniform pore size are of immense interest for applications in catalysis, separation, magnetism, chemical sensing, and optoelectronics.[1] These materials bring together the merits of ordered pore structure with the physical characteristics inherent in inorganic framework. So far, various well-ordered mesoporous transition-metal oxides, such as TiO_2, ZnO_2, SnO_2, ZrO_2, Co_3O_4, Nb_2O_5, and WO_3, and mixed metal oxides, such as $SrTiO_3$, $MgTa_2O_6$, $Co_{0.15}Ti_{0.85}O_{1.85}$, Si(Al, Ti)$O_4$, ZrW_2O_8, and Al_2TiO_5 have been prepared.[2−6] The construction of these mesoporous materials is accomplished using structure-directing molds of soft or hard templates, which permit control over the framework composition and pore geometry (e.g., from wormholes to hexagonal to cubic). Recently, mesoporous materials consisting of different types of components have received significant attention, because of the unusual and potentially useful properties. Compared to mesoporous single-component metal oxides, nanocomposite structures can exhibit enhanced catalytic, magnetic, and electronic properties by coupling disparate components of the framework. Often, it is found that the close interaction between two or more different species can impart complementary or synergistic combinations of properties to the framework, which makes it possible to design novel nanomaterials with specific functionalities.[4−6] Consequently, mesoporous metal-oxide composites are attractive for many applications in redox and photocatalysis, electromagnetism, biosensing, and solar energy conversion.[7,8]

An important and, synchronously, difficult goal in the area of advanced catalytic materials is to design new structural materials that combine high catalytic activity with regular mesoporosity. In this context, porous architectures of well-defined metal–oxygen molecular building units, such as metal-oxide and polyoxometalate compounds, offer interesting and exciting perspectives. Polyoxometalates (POMs), transition metal–oxygen anion clusters (especially of Mo, W, and V) are a large and rapidly growing class of inorganic compounds with unprecedented molecular and compositional diversity. These compounds exhibit fast and reversible multielectron redox transformation and possess remarkable thermal and hydrolytic stability, which make them attractive for applications, especially in acid and oxidation catalysis.[9−12] Mesoporous structures that blend such disparate features are expected to have improved catalytic performance and possess additional characteristics as well, such as fast mass transport kinetics and size-selective absorption.

Several studies have reported the inclusion of polyoxometalates within the mesoporous silica, titania, and alumina framework using surfactant-assisted sol–gel copolymerization of metal oxide and POM species.[13,14] However, despite these successful efforts, the fabrication of mesoporous POM-containing transition-metal oxides with ordered pore structure remains an open challenge. This is because the construction of such complex

Received: June 1, 2011
Revised: July 18, 2011
Published: August 30, 2011

nanostructures requires precise control over the spatial arrangement and cross-linking polymerization of different inorganic oxide species at a mesoscopic level. Furthermore, high thermal stability of the mesostructured framework is required in order to avoid structural collapse after template removal.[15]

Recently, some of us have proposed a hard-templating approach to preparing three-dimensional mesostructured composite frameworks of nanocrystalline Co_3O_4 and Keggin 12-phosphotungstic acids ($H_3PW_{12}O_{40}$).[16] These materials feature a three-dimensional cubic mesostructure derived from the pore structure of silica KIT-6 template, with framework wall composition (i.e., 6−32 wt % in $H_3PW_{12}O_{40}$ loading) appropriate to decompose nitrous oxide into N_2 and O_2. Herein, we extend this approach to the synthesis of well-ordered mesoporous frameworks composed of chromium(III) oxide (Cr_2O_3) and 12-phosphomolybdic acid ($H_3PMo_{12}O_{40}$, PMA) compounds using hexagonal mesoporous SBA-15 silica as hard template. Cr_2O_3 has been widely used as a catalyst for the oxidative dehydrogenation and epoxidation of olefins and decomposition of toluene.[17,18] In particular, we used preformed silica mold to confine the growth of the Cr_2O_3−PMA composite network and imprint mesoporosity after template removal. We demonstrate, for the first time, the feasibility of the proposed synthesis method to achieve high loading of PMA clusters in mesoporous metal-oxide frameworks. These materials, with up to 63 wt % POM content, retain the crystal structure of the silica template. The Cr_2O_3−PMA composites are highly promising catalysts, showing excellent catalytic activity and stability in oxidation of 1-phenylethanol using H_2O_2 as an oxidant.

EXPERIMENTAL SECTION

Synthesis. Hexagonal mesoporous SBA-15 silica was prepared under hydrothermal treatment at 100 °C for 24 h, according to the established procedure.[19] Mesoporous Cr_2O_3 and CrPMA(w) composites were prepared using SBA-15 as a hard template. In a typical synthesis, 0.2 g of SBA-15 silica was dispersed in a clear solution of 2 mL ethanol containing 1 mmol of $Cr(NO_3)_3 \cdot 9H_2O$ and quantitative amount of $H_3PMo_{12}O_{40} \cdot 26H_2O$. The mixture was ultrasonicated (100 kHz, 300 W) at 30 °C until complete ethanol evaporation (∼2 h), and the resulting solid was heated to 300 °C (ramp rate = 1° min^{-1}) for 10 h. The impregnation and decomposition steps were repeated twice to achieve high loading and the obtained material was calcined in air to 400 °C (ramp rate = 1° min^{-1}) for 6 h. The silica template was removed by chemical etching with 5 wt % HF aqueous solution at room temperature. The black material was collected by filtration, washed with water and ethanol several times, and dried at 80 °C for 24 h. A series of mesoporous CrPMA(w) composites (where w refers to the weight percentage of PMA loading in the framework, i.e., w = 18, 30, 39, 52, and 63 wt %) were prepared, using 23, 47, 64, 117, and 165 mg of PMA, respectively. Mesoporous Cr_2O_3 (*meso*-Cr_2O_3) material was prepared in a similar procedure, without the addition of 12-phosphomolybdic acid. Nonporous Cr_2O_3 loaded with 52 wt % PMA, denoted as 52% PMA/Cr_2O_3, was prepared in a similar procedure to CrPMA(52), but without a silica template.

Characterization. Small-angle X-ray scattering (SAXS) patterns were collected on a Rigaku Model S-MAX 3000 high-brilliance system equipped with two-dimensional wire detector and an Cu (λ = 1.54098 Å) rotating anode operated at 80 kV and 40 mA (0.01 $Å^{-1} < q < 0.6$ $Å^{-1}$). Measurements were performed by transmission in samples that were ground and held in a quartz capillary tube (inner diameter (ID) of 1 mm). The sample-to-detector distance and the center of the beam were precisely determined by calibration with Ag-behenate diffraction standard (d_{001} = 58.38 Å). The diffraction intensities of two-dimensional (2D) collected images were integrated to yield one-dimensional (1D) diffraction patterns, as a function of the angle 2θ, with the FIT2D program.[20] Scattering data were corrected for dark current and empty tube scattering. The wide-angle XRD patterns were recorded on a Rigaku Model D/max-2400 X-ray diffractometer (40 kV and 20 mA) equipped with a pyrolytic graphite monochromator giving Cu Kα_1 radiation (λ = 1.5405 Å) in Bragg−Brentano geometry. Data acquisition was performed in the 2θ range of 20°−80° with a scanning step size of 0.02 and count time of 3 s. Nitrogen adsorption−desorption isotherms were measured at 77 K on a Micromeritics Model TriStar II 3020 volumetric analyzer. All the samples were degassed overnight at 130 °C under vacuum (<10^{-5} Torr) prior to measurement. The specific surface areas were calculated using the Brumauer−Emmett−Teller (BET)[21] method on the adsorption data in the relative pressure (P/P_0) range of 0.05−0.20. The total pore volumes were calculated from the adsorbed amount at the relative pressure of 0.95, and the pore size distributions were calculated from the adsorption branch of the isotherms, using the nonlocal density function theory (NLDFT)[22] method. The relative standard deviations of the BET surface area and the total pore volume were <3%. Transmission electron microscopy (TEM) was performed using a JEOL Model JEM-2100 electron microscope equipped with a LaB_6 filament and operated at an accelerated voltage of 200 kV. The samples were first gently ground, ultrasonically dispersed in ethanol, and then picked up on a carbon-coated Formvar copper grid. Elemental microprobe analyses were performed on a JEOL Model JSM-6390LV scanning electron microscopy (SEM) system that was equipped with an Oxford INCA PentaFET-x3 energy-dispersive X-ray spectroscopy (EDS) detector. Data acquisition was performed with an accelerating voltage of 20 kV and an accumulation time of 60 s. Infrared spectra of the samples were recorded with KBr, using a Perkin−Elmer Model Spectrum-BX FT-IR spectrometer. Spectra were obtained on averaging 100 interferograms with a resolution of 2 cm^{-1}. UV/vis diffuse reflectance spectra were taken using a Perkin−Elmer Lambda 950 optical spectrophotometer, using an integrating sphere. A $BaSO_4$ powder was used as a 100% reflectance standard. Reflectance data were converted to absorption (α/S) data, according to the Kubelka−Munk equation:

$$\frac{\alpha}{S} = \frac{(1-R)^2}{2R}$$

where R is the reflectance, α the absorption coefficient, and S the scattering coefficient. X-ray photoelectron spectroscopy (XPS) was performed on an Omicron ESCA system that was equipped with a monochromated Al Kα X-ray (1486.6 eV) source with a 1.5-mm beam diameter and operated at 300 W. A low-energy electron flood gun was employed for charge neutralization. Samples were analyzed at pressures below 2×10^{-8} Torr, with a pass energy of 25 eV and a takeoff angle of 45°. All binding energies were calibrated by assuming the binding energy of the C 1s peak at 284.6 eV. Prior to XPS measurement, the powders were pressed to form a pellet, and then the pellet was put into the entry-load chamber to pump for 2 h. The relative atomic composition was determined from the acquired spectra after background subtraction (linear-type) by integrating the Cr $2p_{3/2}$ and Mo $3d_{5/2}$ peaks and dividing by its sensitivity factor. The sensitivity factors of the Cr $2p_{3/2}$ (7.6) and Mo $3d_{5/2}$ (5.8) signals are provided by spectral data processor (SDP) software v4.3. Peak fitting of XPS spectra was performed using the XPSPEAK v4.1 software.

Catalytic Oxidation of 1-Phenylethanol. The catalytic reactions were carried out in an open cap vial that was equipped with a Teflon septum. The reaction mixture was heated at 50 °C, in the presence of 4 equiv of H_2O_2. In all experiments, HPLC-grade acetonitrile has been used as the solvent. The reaction mixture (2 mL) contained 0.05 M of substrate and an amount of catalyst corresponding to 5×10^{-3} M of $H_3PMo_{12}O_{40}$ for CrPMA(w) and PMA or Cr_2O_3 for

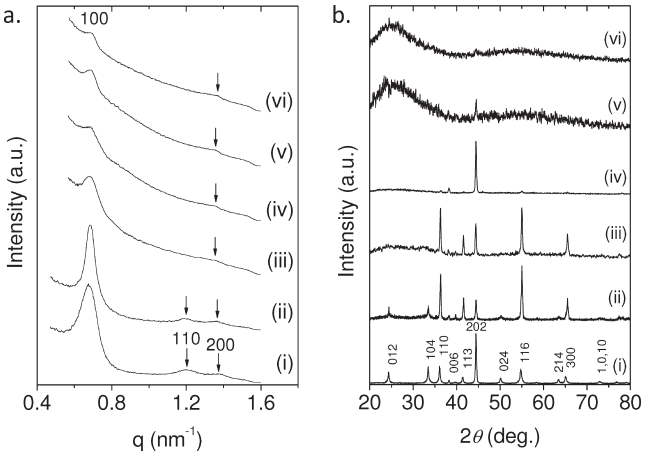

Figure 1. (a) Small-angle X-ray scattering (SAXS) and (b) wide-angle X-ray diffraction (XRD) patterns of mesoporous samples: *meso*-Cr_2O_3 (pattern i), CrPMA(18) (pattern ii), CrPMA(30) (pattern iii), CrPMA(39) (pattern iv), CrPMA(52) (pattern v), and CrPMA(63) (pattern vi). The indexing of the Bragg peaks in XRD is consistent with the rhombohedral structure of Cr_2O_3 (space group: $R\bar{3}c$, lattice constants: $a = b = 0.496$ nm and $c = 1.359$ nm).

meso-Cr_2O_3. The catalytic grains were kept in suspension by vigorous magnetic stirring, and the reaction mixture was monitored by gas chromatography−mass spectrometry (GC-MS) and ^{1}H NMR spectroscopy. Nuclear magnetic resonance (^{1}H NMR and ^{13}C NMR) spectra were recorded on a Bruker Model AMX 300 MHz spectrometer, in $CDCl_3$. Gas chromatography−mass spectroscopy (GC-MS) analysis was performed on a Shimadzu Model GC MSQP5050A apparatus that was equipped with a 30-m HP-5 capillar column and a Model 5971A MS detector.

RESULTS AND DISCUSSION

Synthesis and Structural Characterization. To produce the Cr_2O_3−PMA composites, we used ultrasound-assisted wet impregnation of chromium nitrate ($Cr(NO_3)_3 \cdot 9H_2O$) and PMA precursors into the pore channels of SBA-15 silica.[23] This process was found to be the key in producing mesostructured solid-solution frameworks with high loading of PMA clusters and large internal surface area. By adjusting the quantity of 12-phosphomolybdic acid, mesoporous structures feature different loading of PMA, ranging from 18 wt % to 63 wt %. Ordered mesoporous CrPMA(w)—where w is the weight percentage content of PMA—were obtained after inverse replica solidification of chromium oxide, following removal of the silica template through chemical etching with HF solution.

The chemical composition of mesoporous replicas was determined with energy-dispersive X-ray spectroscopy (EDS). Elemental EDS data for CrPMA(w) indicated the expected PMA content from the stoichiometry of reactions (that is, 18, 30, 39, 52, and 63 wt %; see Table S1 in the Supporting Information). This implies that the chromium nitrate and PMA precursors were fully incorporated into the pores of SBA-15, as well as the as-prepared mesostructures are stable for PMA leaching in aqueous HF solution. Meanwhile, the absence of any trace of silicon in EDS spectra suggests the complete elimination of the silica mold.

The mesoscopic order of the title materials was investigated with small-angle X-ray scattering (SAXS) and transmission electron microscopy (TEM). The SAXS patterns of the mesoporous Cr_2O_3 and CrPMA(18) samples show three intense diffraction peaks in the scattering vector q ($q = 4\pi \sin(\theta/\lambda)$,

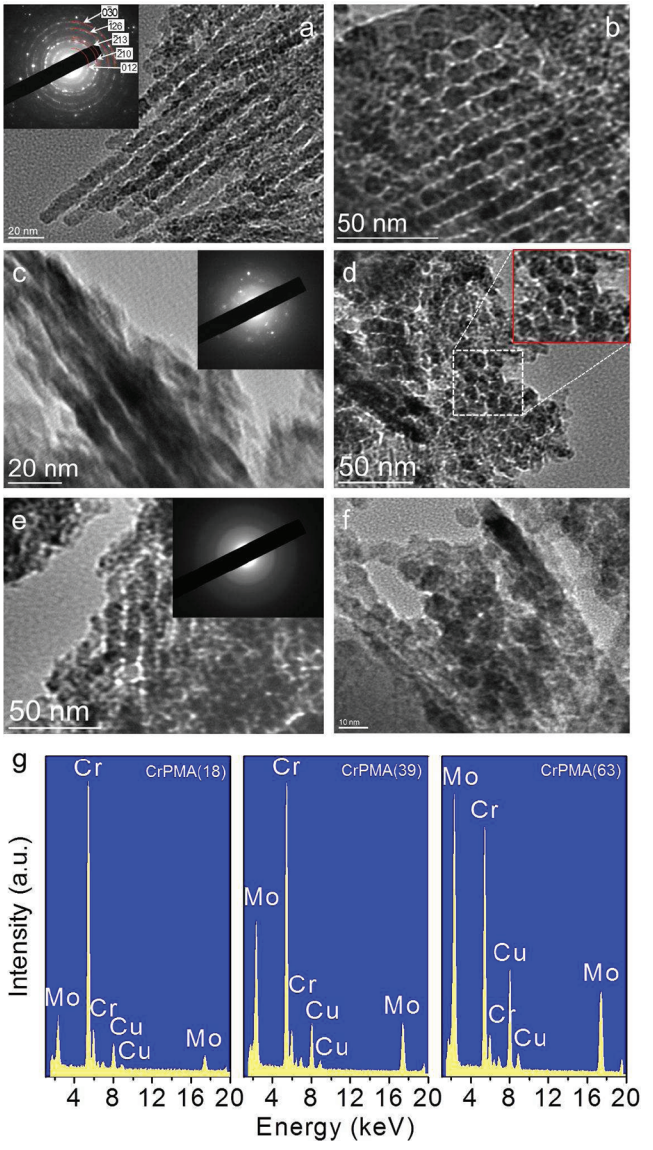

Figure 2. (a−f) TEM images of mesoporous CrPMA(18) (panels a and b), CrPMA(39) (panels c and d), and CrPMA(63) (panels e and f), viewed along the [110]-direction (left) and along the [001]-direction (right panel) of the hexagonal structure. Inset in each micrograph shows the corresponding SAED pattern. (g) TEM-EDS spectra of mesoporous CrPMA(18), CrPMA(39), and CrPMA(63) samples. The copper peaks result from the TEM Cu grid.

where 2θ is the scattering angle) range of 0.6−1.4 nm^{-1}, which can be attributed to the 100, 110, and 200 Bragg reflections of the hexagonal *p6mm* symmetry (see Figure 1a). These SAXS profiles are similar to that of SBA-15 (see Figure S1 in the Supporting Information), suggesting that thus-prepared replicas maintain the highly ordered mesostructure of the silica template. However, a decrease of the structural ordering with increasing the PMA content is inferred for high-PMA-loading CrPMA(w) (w = 30, 39, 52, and 63 wt %) samples, judging from the lower intensity of the 100 and 200 diffractions and the absence of the 110 diffraction peak. The angular position of the 100 diffractions is associated with an interplanar distance ($d = 2\pi/q$) of $d \approx$ 9.1−9.2 nm, which gives a hexagonal lattice parameter (a_0) at ∼10.5−10.6 nm. These lattice parameters are almost equal to

that of the pristine SBA-15 (10.6 nm), indicating perfect replication of the silica porous structure.

The wide-angle X-ray diffraction (XRD) patterns, in Figure 1b, display several sharp diffraction peaks for mesoporous Cr_2O_3 and CrPMA(18), which can be indexed to the rhombohedra $R\bar{3}c$ symmetry of Cr_2O_3 with lattice parameters $a = b = 0.496$ nm and $c = 1.359$ nm (Internation Centre for Diffraction Data (ICDD) Powder Diffraction File (PDF) Card No. 82-1484).[24] The well-resolved XRD diffractions suggest that the chromium nitrate precursor was completely converted to crystalline Cr_2O_3.[25] Surprisingly, the CrPMA composites loaded with 30−63 wt % of PMA show a systematic decrease in the relative intensity of X-ray reflections that is indicative of lower Cr_2O_3 crystallinity. Indeed, the wall structure of the CrPMA(52) and CrPMA(63) compounds lacked long-range atomic order, as indicated by the absence of Bragg diffractions in wide-angle XRD. It is likely that the PMA clusters are well-mixed with chromium oxide compounds, leading to restrictions in the formation of Cr_2O_3 crystallites during the heat-treatment process. The absence of $H_3PMo_{12}O_{40}$ crystalline phase in wide-angle XRD patterns supports evidence that the PMA clusters are homogeneously dispersed in mesoporous frameworks. However, the presence of too low amounts of nanometer-sized PMA aggregates within the mesoporous samples cannot be excluded.

Figures 2a−f display typical TEM images of mesoporous CrPMA(18), CrPMA(39), and CrPMA(63). The TEM images of CrPMA(18) and CrPMA(39) samples depict a well-ordered arrangement of uniform nanorods in hexagonal symmetry. However, such structural ordering is barely attained on CrPMA-(63), where a rather irregular mesostructure is indicated. Detailed analysis of TEM images suggested that the as-obtained nanorods have a cross-section size of ∼7 nm, which reflect the mesopore diameter of SBA-15 (ca. 7.2 nm; see Figure S2 in the Supporting Information). The crystalline nature of the framework walls is further investigated with selected-area electron diffraction (SAED), indicating a varying degree of Cr_2O_3 crystallinity that strongly related to the PMA content (Figures 2a−f, insets). In particular, the CrPMA(18) sample exhibits a well-defined multicrystalline diffraction pattern, showing a series of spotted Debye−Scherrer diffraction rings. These diffractions are indexed, most closely, according to the rhombohedral $R\bar{3}c$ structure of Cr_2O_3. However, the mesoporous CrPMA(39) sample exhibits a poorly crystalline diffraction pattern that corresponds to the semicrystalline Cr_2O_3 phase, while the CrPMA(63) exhibit broad and diffusive scattering rings characteristic of amorphous structure. These results are consistent with the wide-angle XRD data. Elemental TEM-EDS analysis acquired on a thin area of mesoporous frameworks indicated a homogeneous distribution of Cr and Mo elements with Cr/Mo atomic ratio that corresponds to PMA loadings of ∼17.2, ∼38.3, and ∼61.2 wt % for the CrPMA(18), CrPMA(39), and CrPMA-(63) samples, respectively, as expected from the nominal compositions (see Figure 2g).

The nitrogen physisorption measurements of silica-free replicas show Type IV isotherms with a pronounced condensation step in the relative pressure (P/P_0) range of ∼0.2−0.3, especially for pure Cr_2O_3 and CrPMA(w) composites with low PMA content (w = 18, 30, and 39 wt %), indicating narrow-sized mesopores (see Figure 3). The lack of a hysteresis loop between the adsorption and desorption branches of *meso*-Cr_2O_3 and CrPMA(18) indicates negligible pore blocking effects and corroborates the tubular pore structure. While the peculiar H_2-type

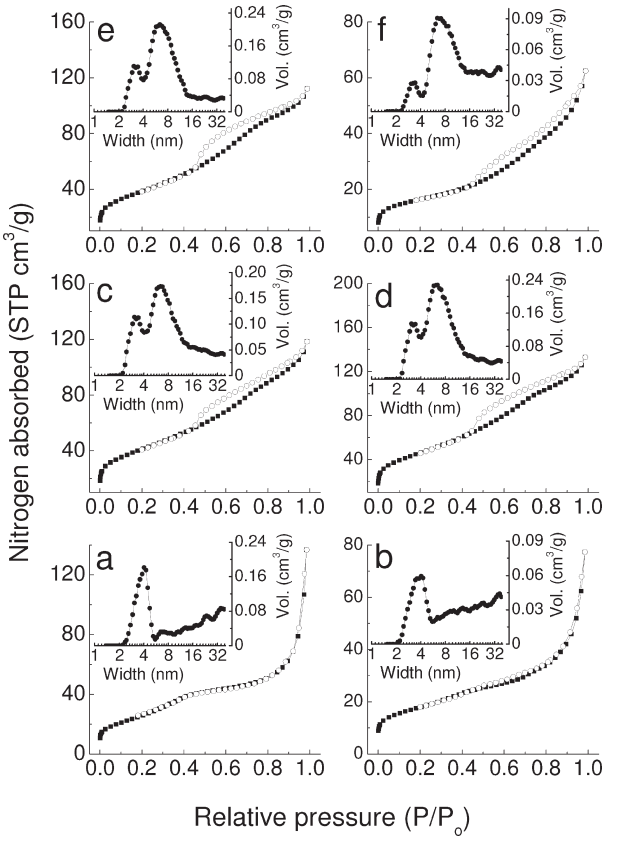

Figure 3. Nitrogen adsorption (closed symbols) and desorption (open symbols) isotherms at 77 K of mesoporous (a) *meso*-Cr_2O_3, (b) CrPMA(18), (c) CrPMA(30), (d) CrPMA(39), (e) CrPMA(52), and (f) CrPMA(63). The NLDFT pore size distributions calculated from the adsorption branches are shown in the insets.

hysteresis loop observed for high-PMA-loading CrPMA(w) (w = 30−63 wt %) samples implies, rather, the presence of an interconnected pore network with large mesopores (4−12 nm).[26] The small uptake of the adsorption isotherms at $P/P_0 > 0.8$ is associated with the capillary condesation of nitrogen in large voids between the particles. Such an interparticle porosity presumably originates because of the large volume contraction from $Cr(NO_3)_3 \cdot 9H_2O$ precursor to Cr_2O_3 oxide (ca. 64.6%, based on mass density) that results in incomplete filling of the SBA-15 nanopores. The mesoporous Cr_2O_3 exhibited a BET surface area of 99 $m^2\ g^{-1}$ and a total pore volume of 0.13 $cm^3\ g^{-1}$, which is one of the largest observed so far for this system. However, the mesoporous CrPMA(w) composites exhibited BET surface areas in the range of 58−165 $m^2\ g^{-1}$ and total pore volumes in the range of 0.08−0.19 $cm^3\ g^{-1}$. The surface area of CrPMA(w) increased as the loading of PMA was increased from 18 wt % to 39 wt %, possibly because of the lower density of included PMA clusters (4.0 g cm^{-3}), compared to that of chromium oxide (5.2 g cm^{-3}). The reduction of the surface area and pore volume for CrPMA(52) and CrPMA(63) can be attributed to the rather irregular pore structure, because of the incomplete interconnection of nanorods (see below). Given the heavier elements that compose the frameworks, these surface areas are reasonable and correspond to silica equivalent surface areas of 117−356 $m^2\ g^{-1}$.

Pore size distribution analysis with the nonlocal density functional theory (NLDFT) shows one maximum at ∼4 nm for mesoporous Cr_2O_3 and CrPMA(18) and two maxima at

dx.doi.org/10.1021/cm201547r |*Chem. Mater.* 2011, 23, 4204–4211

Table 1. Textural Properties of Mesoporous Cr_2O_3 (*meso*-Cr_2O_3) and CrPMA(w) Composites

sample	surface area[a] ($m^2\ g^{-1}$)	pore volume[b] ($cm^3\ g^{-1}$)	pore size (nm)	d_{100}-spacing (nm)	unit cell[c] (nm)	wall thickness, WT[d] (nm)
meso-Cr_2O_3	99 (235)	0.13	4.1	9.267	10.6	6.5
CrPMA(18)	64 (145)	0.08	3.9	9.159	10.6	6.7
CrPMA(30)	147 (324)	0.16	3.3, 6.5	9.186	10.6	7.3
CrPMA(39)	165 (356)	0.19	3.3, 6.4	9.146	10.6	7.3
CrPMA(52)	138 (288)	0.16	3.3, 6.4	9.132	10.5	7.2
CrPMA(63)	58 (117)	0.08	3.3, 6.9	9.093	10.5	7.2

[a] Values given in parentheses indicate the silica equivalent surface areas, based on skeletal mass density (i.e., the ratio of the mass to the volume occupied by the sample excluding the volume of interparticle voids and any open pores) calculations and assuming skeletal density of silica, Cr_2O_3, and PMA (equal to 2.2, 5.2, and 4.0 g cm^{-3}, respectively). [b] Cumulative pore volume at $P/P_0 = 0.95$. [c] The unit-cell parameter, given by $a_0 = (2/\sqrt{3})d_{100}$. [d] The framework wall thickness given by WT = $a_0 - D_p$, where D_p is the pore size. The standard deviations of unit-cell size and framework wall thickness are each ±0.1 nm.

~3.3 nm and ~6.5−7 nm for high-PMA-loading CrPMA(w) (w = 30−63 wt %) samples (Figure 3, insets). The pore size at ~3−4 nm comes from the wall thickness of the silica template (ca. 3 nm; see Figure S2 in the Supporting Information), whereas the latter (ca. 7 nm) is attributed to the large voids between partially interconnected nanorods. Considering the large diameter of phosphomolybdates (~1.3 nm),[27] the PMA clusters may block the small-sized complementary pores (<1 nm) within the silica walls after infiltration. In this case, the interconnectivity between the adjacent mesopores is low (because of the closed complementary channels); therefore, the original structural symmetry cannot be well-retained after the template removal. The pore size obtained from the NLDFT analysis, together with the pore-to-pore distance (a_0) obtained from XRD data, indicate a framework wall thickness of ~6.5−7 nm, which is in very good agreement with that observed from TEM. Table 1 summarizes all the textural parameters of mesoporous Cr_2O_3 and CrPMA(w) materials.

Spectroscopy. The structure of mesoporous Cr_2O_3 and CrPMA-(w) composite was also studied by Fourier transform-infrared (FT-IR) and diffuse reflectance ultraviolet−visible (UV/vis) spectroscopy. The FT-IR spectra of CrPMA(w) show the characteristic absorption peaks at ~947 and ~879 cm^{-1}, which correspond to ν_{as}(Mo═O_d) and ν_{as}(Mo−O_b−Mo) stretching vibration bands of PMA Keggin cluster, respectively (see Figure S3 in the Supporting Information).[28] Compared with the bulk PMA, these vibration bands are bathochromic/red-shifted by more than 5−20 cm^{-1}, which is assigned to the strong conjugated interactions between the terminal (Mo═O_d) and bridged (Mo−O_b−Mo) oxygen atoms of PMA polyanions and chromium oxide matrix. The intense absorption at ~1077 cm^{-1} can be ascribed to ν_{as}(P−O_a) stretching mode of distorted PO_4 central unit. These results support that the Keggin structure of PMA is retained intact within the composite frameworks.

The diffuse reflectance UV/vis spectra of mesoporous CrPMA-(w) show an absorption peak at ~316−318 nm, which corresponds to the O(−II)→Mo(VI) charge-transfer in Mo−O−Mo bond of the PMA clusters (see Figure S4 in the Supporting Information).[29] This absorption exhibits a remarkable bathochromic shift, with respect to the bulk PMA (~302 nm), possible due to the binding of molecular PMA units to the chromium oxide network. All the CrPMA(w) samples showed a broad absorption peak at ~468−470 nm and a weak shoulder at ~513−516 nm, which can be assigned to the crystal-field d−d transitions ($^4A_{2g}\rightarrow{}^4T_{1g}$) of 6-fold coordinated Cr(III) in Cr_2O_3.[30] The optical spectrum of mesoporous Cr_2O_3 suggests the potential presence of Cr(VI) species within the Cr_2O_3. In particular, the absorption peak at ~348 is assigned to the ligand−metal charge transfer O(−II)→Cr(VI) process and the feature at ~598 nm is attributed to the $^4A_{2g}\rightarrow{}^4T_{2g}$ transition of Cr(III) in octahedral symmetry.[31] These peaks are hardly observed in mesoporous CrPMA(w), because of the strong absorptions by the PMA heteropoly acids.

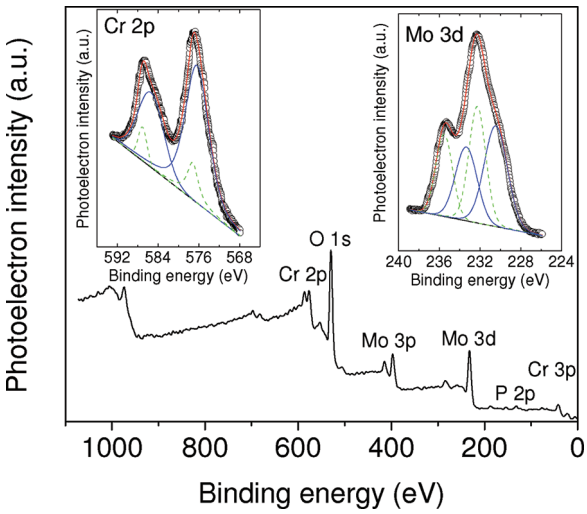

Figure 4. X-ray photoelectron spectroscopy (XPS) spectrum of mesoporous CrPMA(63), showing the characteristic peaks of Cr, Mo, P and O. The insets show high-resolution Mo $3d_{5/2}$−$3d_{3/2}$ and Cr $2p_{3/2}$−$2p_{1/2}$ core-level photoelectron spectra (open circles represent raw data, red lines denote fitted lines, and blue/green lines represent deconvoluted lines).

XPS experiments were performed to probe the chemical state of the Cr and Mo atoms in mesoporous frameworks. Figure 4 shows the XPS survey spectrum and high-resolution XPS spectra of Cr 2p and Mo 3d core-level signals for CrPMA(63). The Cr 2p XPS spectrum could be resolved in two sets of spin−orbit doublets of Cr $2p_{3/2}$ and $2p_{1/2}$ signals, which leads to a reliable fitting. Although the peaks at 576.3 and 585.4 eV were referred to Cr(III) ions, the second doublet at 577.2 and 587.0 eV was ascribed to the presence of Cr(IV) and/or Cr(III) hydroxyl species (i.e., $Cr(OH)_3$) within the Cr_2O_3 oxide.[32,33] The XPS deconvoluted peaks of Mo $3d_{5/2}$ and $3d_{3/2}$ with binding energies at 232.4 and 235.6 eV are attributed to high-valence Mo(VI) and those at 230.4 and 233.4 eV are attributed to reduced Mo(V) ions, respectively.[34] Generally, the binding energy of an atom increases as the oxidation state increases.[35] Based on the area contributions and sensitivity factors of Cr $2p_{3/2}$ and Mo $3d_{5/2}$

dx.doi.org/10.1021/cm201547r |*Chem. Mater.* 2011, 23, 4204–4211

Table 2. Oxidation of 1-Phenylethanol with 30% H_2O_2 Catalyzed by Mesoporous Cr_2O_3 (*meso*-Cr_2O_3) and CrPMA(w) Composites and Homogeneous PMA Compound[a]

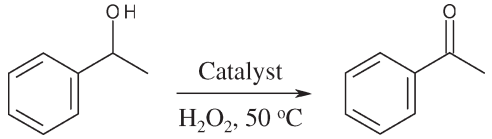

catalyst	conversion[b] (%)	turnover frequency, TOF[c] (h^{-1})
meso-Cr_2O_3	10	11
CrPMA(18)	22	22
CrPMA(30)	36	43
CrPMA(39)	51	72
CrPMA(52)	85 (54)[d]	105 (67)[d]
CrPMA(63)	87	103
PMA	9	10

[a] Reaction conditions: 0.1 mmol of 1-phenylethanol, 0.01 mmol of catalyst, 4 equivalent of H_2O_2 (30% aqueous), 2 mL CH_3CN, 50 °C, 5 min. [b] Conversion is given in terms of mol % of initial quantity of oxidant used. [c] Turnover frequency (TOF) is based on the number of moles of 1-phenylethanol converted per mole of $H_3PMo_{12}O_{40}$ (Cr_2O_3 for *meso*-Cr_2O_3) per unit time. [d] Conversion and TOF of a nonporous 52% PMA/Cr_2O_3 solid.

peaks, the Cr/Mo atomic ratio was estimated to be 53:47, which gives a weight percentage of PMA content at ~64 wt %, in very good agreement with the EDS results.

Catalytic Activity. The catalytic activity of mesoporous replicas has been assessed by studying the oxidation of 1-phenylethanol as a model reaction. The selective oxidation of nonactivated alcohols, such as allylic and alicyclic alcohols, under mild conditions is a challenging issue for production of fine chemicals and pharmaceuticals.[36] All the heterogeneous catalytic reactions were carried out under the same conditions, using 0.05 M of alcohol and an amount of mesoporous replicas corresponding to 5×10^{-3} M of PMA for CrPMA(w) or Cr_2O_3 for *meso*-Cr_2O_3, and an excess of hydrogen peroxide as an oxidant (4 equiv, based on alcohol amount).[37] The CrPMA(w) composites are good catalysts for the selective oxidation of 1-phenylethanol, affording moderate to excellent yield of acetophenone within a short reaction time. As shown in Table 2, the catalytic activity is highly dependent on the amount of included PMA clusters and increases with increasing PMA loading. Indeed, the CrPMA catalysts loaded with 52 and 63 wt % of PMA achieved excellent conversion (ca. 85%−87%) and selectivity (100%) within only 5 min. Interestingly, these catalysts convert 1-phenylethanol to acetophenone in almost quantitative yields (>96%) within 10 min. No byproducts, such as benzoic acid or ethylbenzene, were detected under the investigated conditions. The pseudo-first-order reaction rate, together with the high reaction rate constants indicated for the CrPMA(52) ($k = 0.283\ min^{-1}$) and CrPMA(63) ($k = 0.325\ min^{-1}$) catalysts, suggests that the reaction proceeds very fast via the formation of a metal-peroxo complex (e.g., Mo−O−O−H), followed a rate-determining step of 1-phenylethanol oxidation (see Figure S5 in the Supporting Information). Among the catalysts tested, the CrPMA(52) sample was found to be the most effective for the oxidation of 1-phenylethanol, giving a higher turnover frequency (TOF) of 103 h^{-1}. The catalytic efficiency of the CrPMA(52) sample exceeds the efficiency of other high-performance catalysts that were reported to be active in oxidation

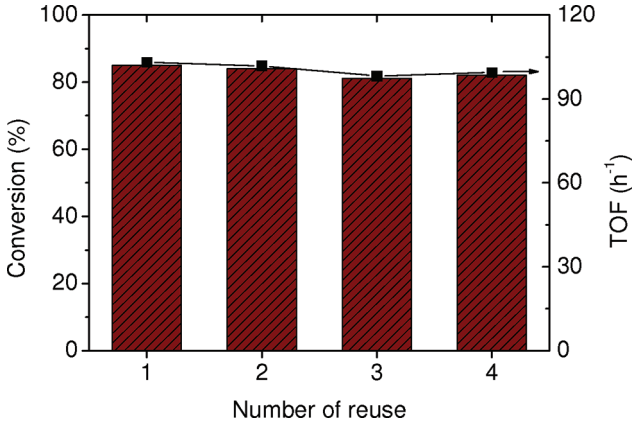

Figure 5. Recycle studies of mesoporous CrPMA(52) catalyst. (Reaction conditions: 0.1 mmol of 1-phenylethanol, 0.01 mmol of catalyst, 4 equiv of H_2O_2 (30% aqueous), 2 mL CH_3CN, 50 °C, 5 min.)

of 1-phenylethanol, but in prolonged time, at high temperature, and/or in the presence of harmful bases as co-catalysts (e.g., KOH, pyridine). These include the homogeneous $[LMn(\mu\text{-}O)_3MnL](PF_6)_2$ and $[LMn(\mu\text{-}O)_3MnL]_2[SiW_{12}O_{40}]$, where L is 1,4,7-trimethyl-1,4,7-triazacyclononane) (~94%−95% conv. in 3 h),[38] $Os_3(CO)_{10}(\mu\text{-}H)_2$ (~60% conv. in 10 h),[39] and $[(C_{12}H_{13}NO)Pb(OAc)]_2$ (~99% conv. with pyridine in 24 h)[40] compounds, the Pd and Pt (~98% conv. in 24 h)[41] nanoclusters and the Au/TiO_2, Au/CeO_2, Au/SiO_2, and Au/MgO (~18%−99% conv. in 3−10 h),[42] $Au_{70}Pb_{30}/TiO_2$ (~98% conv. in 0.5 h at 90 °C),[43] $Au/Ga_3Al_3O_9$ (~99% conv. in 15 h)[44] and Pd/SBA-15 (~97% conv. in 10 h)[45] nanocomposites. These results clearly support the superior catalytic performance of the CrPMA(52) material in the oxidation of nonactivated alcohols, such as 1-phenylethanol.

For comparison, the corresponding homogeneous reaction was also carried out, under the same conditions described above. In all cases, the heterogeneous reactions were found to proceed faster than the corresponding homogeneous. The results, in Table 2, demonstrate the superior catalytic activity of mesoporous CrPMA(w) composites, compared to the homogeneous PMA compound or even to the mesoporous Cr_2O_3. Note that no oxidation products were observed when blank experiments were run in the absence of a catalyst. The enhanced catalytic activity can be regarded as a result of synergetic interactions between the PMA clusters and Cr_2O_3 matrix (e.g., via Cr−O−Mo bonds). Nevertheless, the good dispersion of PMA and large efficient surface area are also other important parameters which cannot be definitively ruled out. To examine the role of ordered mesostructure on catalytic performance, we also prepared Cr_2O_3 catalyst loaded with 52 wt % of PMA (52% PMA/Cr_2O_3), which is similar to CrPMA(52), but without a silica template. The 52% PMA/Cr_2O_3 compound possesses a bulklike, nonporous, structure (BET surface area ≈ 5.5 $m^2\ g^{-1}$) and its catalytic activity was studied under the same reaction conditions. Interestingly, this material exhibited moderate catalytic activity (~54% conversion, TOF ≈ 67 h^{-1}) that is remarkably lower than that of the CrPMA(52) sample, probably because of the lower reaction rate causing the smaller efficient surface area and disordered pore structure.

Furthermore, the CrPMA(52) catalyst can be reused four times without a significant loss of catalytic activity (~81%−85% conversion, ~98−103 h^{-1} TOF) and selectivity (100%), see

Figure 5. After each catalytic run, the catalyst was isolated by filtration, washed with acetonitrile, and dried under ambient conditions. Elemental EDS microanalysis and FT-IR spectroscopy corroborate the retention of PMA Keggin units within the mesoporous structure of reused sample, thereby confirming high durability and recyclability. The EDS spectra showed average Cr/P/Mo atomic ratios of ~22.1:1.3:12, which correspond to a PMA content of ~52.1 wt %, which is almost equal to that of fresh catalyst (~52.4 wt %). The FT-IR spectra displayed the characteristic $\nu_{as}(Mo{=}O_d)$ and $\nu_{as}(Mo{-}O_b{-}Mo)$ vibration bands at ~946 and ~880 cm^{-1} respectively, reflecting the Keggin structure of the 12-phosphomolybdic acids (see Figure S6 in the Supporting Infomation).

CONCLUSIONS

In summary, we have successfully prepared novel mesoporous Cr_2O_3−phosphomolybdic acid (PMA) solid solution frameworks through an ultrasound-assisted hard-templating approach. This method represents an important step toward the synthesis of ordered mesoporous transition-metal oxides loaded with large amount of POM clusters. The resulting materials possess Cr_2O_3−PMA framework composition with different PMA cluster contents, ranging from 18 wt % to 63 wt %. The composites displayed three-dimensional (3D) hexagonal structure, high surface area (58−165 $m^2\,g^{-1}$), and large mesopores (ca. 3−4 and 7 nm). These materials have important implications for oxidative catalytic processes including H_2O_2-mediated oxidation of 1-phenylethanol. The CrPMA composites, we report here, undergo very fast oxidation of 1-phenylethanol (within 5 min) with high catalytic activity (ca. 85% −87%) and selectivity (100%), and show very good recyclability and durability. The easy separation from the reaction mixture, along with the high activity, stability, and retained activity in subsequent catalytic cycles, makes these materials suitable for small-scale synthesis. For this reason, further extension of the present synthesis method to other mesoporous POM-containing transition-metal oxides as "green" catalysts is currently being explored.

ASSOCIATED CONTENT

Supporting Information. Analytical data of mesoporous CrPMA(w) composites, SAXS pattern, N_2 adsorption−desorption isotherms at 77 K and NLDFT pore size distribution of mesoporous SBA-15, FT-IR and diffuse reflectance UV/vis spectra of mesoporous *meso*-Cr_2O_3 and CrPMA(w), kinetic profiles of CrPMA(52) and CrPMA(63) catalysts, and FT-IR spectrum of four-times-reused CrPMA(52) catalyst. This material is available free of charge via the Internet at http://pubs.acs.org.

AUTHOR INFORMATION

Corresponding Author

*Tel.: 0030-2810-545004. E-mail: garmatas@materials.uoc.gr.

Present Addresses

$^{\nabla}$Department of Chemistry, Aristotle University of Thessaloniki, Thessaloniki 54124, Greece.

ACKNOWLEDGMENT

We thank M. Kanatzidis from Chemistry Department, Northwestern University (Evanston IL, USA) for nitrogen physisorption and SAXS measurements. Financial support from the European Community under the Marie-Curie International Reintegration Grand (No. 230868) is gratefully acknowledged.

REFERENCES

(1) Davis, M. E. *Nature* **2002**, *417*, 813.
(2) Yang, P.; Deng, T.; Zhao, D.; Feng, P.; Pine, D.; Chmelka, B. F.; Whitesides, G. M.; Stucky, G. D. *Science* **1998**, *282*, 2244.
(3) (a) Carreon, M. A.; Guliants, V. V. *Eur. J. Inorg. Chem.* **2005**, *1*, 27. (b) Vasylyev, M. V.; Neumann, R. *J. Am. Chem. Soc.* **2004**, *126*, 884.
(4) Zen, H.; Li, J.; Liu, J. P.; Wang, Z. L.; Sun, S. *Nature* **2002**, *420*, 395.
(5) Mamak, M.; Coombs, N.; Ozin, G. *J. Am. Chem. Soc.* **2000**, *122*, 8932.
(6) Vayssilov, G. N.; Lykhach, Y.; Migani, A.; Staudt, T.; Petrova, G. P.; Tsud, N.; Skala, T.; Bruix, A.; Illas, F.; Prince, K. C.; Matolin, V.; Neyman, K. M.; Libuda, J. *Nat. Mater.* **2011**, *10*, 310.
(7) Li, D.; Zhou, H.; Honma, I. *Nat. Mater.* **2004**, *3*, 65.
(8) Grosso, D.; Boissiere, C.; Smarsly, B.; Brezesinski, T.; Pinna, N.; Albouy, P. A.; Amenitsch, H.; Antonietti, M.; Sanchez, C. *Nat. Mater.* **2004**, *3*, 787.
(9) Kozhevnikov, I. V. *Catalysis for Fine Chemical Synthesis: Catalysis by Polyoxometalates*; Wiley−VCH: Chichester, U.K., 2002.
(10) Tzirakis, M. D.; Lykakis, I. N.; Orfanopoulos, M. *Chem. Soc. Rev.* **2009**, *38*, 2609.
(11) Hill, C. L. *Chem. Rev.* **1998**, *98*, 1(special issue devoted to polyoxometalates).
(12) Hiskia, A.; Mylonas, A.; Papaconstantinou, E. *Chem. Soc. Rev.* **2001**, *30*, 62.
(13) Vasylyev, M.; Neumann, R. *J. Am. Chem. Soc.* **2004**, *126*, 884.
(14) Nishiyama, Y.; Nakaqawa, Y.; Mizuno, N. *Angew. Chem., Int. Ed.* **2001**, *40*, 3639.
(15) Yang, P.; Zhao, D.; Margolese, D. I.; Chmelka, B. F.; Stucky, G. D. *Nature* **1998**, *396*, 152.
(16) Armatas, G. S.; Katsoulidis, A. P.; Petrakis, D. E.; Pomonis, P. J.; Kanatzidis, M. G. *Chem. Mater.* **2010**, *22*, 5739.
(17) Wang, S. B.; Murata, K.; Hayakawa, T.; Hamakawa, S.; Suzuki, K. *Catal. Lett.* **1999**, *63*, 59.
(18) Sinha, A. K.; Suzuki, K. *Angew. Chem. Ind. Ed.* **2005**, *44*, 271.
(19) Zhao, D.; Huo, Q.; Feng, J.; Chmelka, B. F.; Stucky, G. D. *J. Am. Chem. Soc.* **1998**, *120*, 6024.
(20) Hammersley, F. A. P. *ESRF98HA01T: FIT2D V9.129 Reference Manual V3.1*; ESRF−Internal Report: France, 1998.
(21) Brunauer, S.; Deming, L. S.; Deming, W. S.; Teller, E. *J. Am. Chem. Soc.* **1940**, *62*, 1723.
(22) Ravikovitch, P. I.; Wei, D.; Chueh, W. T.; Haller, G. L.; Neimark, A. V. *J. Phys. Chem. B* **1997**, *101*, 3671.
(23) Deng, J.; Zhang, L.; Dai, H.; Xia, Y.; Jiang, H.; Zhang, H.; He, H. *J. Phys. Chem. C* **2010**, *114*, 2694.
(24) McMurdie, H. F.; Morris, M. C.; Evans, E. H.; Paretzkon, B.; Wong-Ng, W.; Zhang, Y.; Hubbard, C. R. *Powder Diffr.* **1987**, *2*, 45.
(25) Dickinson, C.; Zhou, W.; Hodgkins, R. P.; Shi, Y.; Zhao, D.; He, H. *Chem. Mater.* **2006**, *18*, 3088.
(26) Thommes, M.; Köhn, R.; Fröba, M. *Appl. Surf. Sci.* **2002**, *196*, 239.
(27) Boeyens, J. C. A.; McDougal, J. G.; van Smit, J. *J. Solid State Chem.* **1976**, 18191.
(28) Rocchiccioli-Deltcheff, C.; Thouvenot, R.; Franck, R. *Spectrochim. Acta A* **1976**, *32*, 578.
(29) Lopez-Salinas, E.; Hernandez-Cortez, J. G.; Cortez, M.; Navarrete, J.; Yanos, M.; Vazquez, A.; Armendaris, H.; Lopez, T. *Appl. Catal.* **1998**, *175*, 43.
(30) Zhu, Z.; Chang, Z.; Kevan, L. *J. Phys. Chem. B* **1999**, *103*, 2680.
(31) Li, L.; Yan, Z. F.; Lu, G. Q.; Zhu, Z. H. *J. Phys. Chem. B* **2006**, *110*, 178.
(32) Tsutsumi, T.; Ikemoto, I.; Namikawa, T.; Kurosa, H. *Bull. Chem. Soc. Jpn.* **1981**, *54*, 913.

(33) Capece, F. M.; Dicastro, V.; Furlani, C.; Mattogno, G.; Fragale, C.; Gargano, M.; Rossi, M. *J. Electron Spectrosc. Relat. Phenom.* **1982**, *27*, 119.
(34) Hasik, M.; Pron, A.; Pozniczek, J.; Bielanski, A.; Piwowarska, Z.; Kruczala, K.; Dziembaj, R. *J. Chem. Soc. Faraday Trans.* **1994**, *90*, 2099.
(35) O'Connor, D. J.; Sexton, B. A.; Smart, R. St. C. X-ray Photoelectron Spectroscopy In *Surface Analysis Methods in Materials Science*; Springer: Berlin, 2003; Ch. 7, pp 175−201.
(36) Mallat, T.; Baiker, A. *Chem. Rev.* **2004**, *104*, 3037.
(37) Strukul, G. *Catalytic Oxidations with Hydrogen Peroxide as Oxidant*; Kluwer Academic Publishers: Dordrecht, The Netherlands, 1992.
(38) Shul'pin, G. B.; Kozlov, N.; Shul'pina, L. S.; Strelkova, T. V.; Mandelli, D. *Catal. Lett.* **2010**, *138*, 193.
(39) Shul'pin, G. B.; Kozlov, Y. N.; Shul'pina, L. S.; Petrovskiy, P. V. *Appl. Organometal. Chem.* **2010**, *24*, 464.
(40) Paavola, S.; Zetterberg, K.; Privalov, T.; Csoregh, I.; Moberg, C. *Adv. Synth. Catal.* **2004**, *346*, 237.
(41) Wang, T.; Xiao, C.-X.; Yan, L.; Xu, L.; Luo, J.; Shou, H.; Kou, Y.; Liu, H. *Chem. Commun.* **2007**, 4375.
(42) Mitsudome, T.; Noujima, A.; Mizugaki, T.; Jitsukawa, K.; Kaneda, K. *Adv. Synth. Catal.* **2009**, *351*, 1890.
(43) Frank, A. J.; Rawski, J.; Maly, K. E.; Kitaev, V. *Green Chem.* **2010**, *12*, 1615.
(44) Su, F.-Z.; Liu, Y.-M.; Wang, L.-C.; Cao, Y.; He, H.-Y.; Fan, K.-N. *Angew. Chem., Int. Ed.* **2008**, *47*, 334.
(45) Ma, Z.; Yang, H.; Qin, Y.; Hao, Y.; Li, H. *J. Mol. Catal. A: Gen.* **2010**, *331*, 78.